

Active Polarization Descattering

Tali Treibitz, *Student Member, IEEE*, and Yoav Y. Schechner, *Member, IEEE*

Abstract—Imaging in scattering media such as fog and water is important but challenging. Images suffer from poor visibility due to backscattering and signal attenuation. Most prior methods for scene recovery use active illumination scanners (structured and gated), which can be slow and cumbersome. On the other hand, natural illumination is inapplicable to dark environments. This paper addresses the need for a non-scanning recovery method which uses active scene irradiance. We study the formation of images under wide-field artificial illumination. Based on the formation model, this paper presents an approach for recovering the object signal. It also yields rough information about the 3D scene structure. The approach can work with compact simple hardware, having active wide-field polychromatic polarized illumination. The camera is fitted with a polarization analyzer. Two frames of the scene are instantly taken, with different states of the analyzer or light-source polarizer. A recovery algorithm follows the acquisition. It allows both the backscatter and the object reflection to be partially polarized. It thus unifies and generalizes prior polarization-based methods, which had assumed exclusive polarization of either of these components. The approach is limited to an effective range due to image noise and falloff of wide-field illumination. Thus, these limits and the noise sensitivity are analyzed. The approach particularly applies underwater. We therefore use the approach to demonstrate recovery of object signals and significant visibility enhancement in underwater field experiments.

Index Terms—Computer vision, modeling and recovery of physical attributes, scene analysis—color, physics-based vision, vision in scattering media, inverse problems, polarization, image recovery.

1 INTRODUCTION

SCATTERING media exist in bad weather, liquids, biological tissue, and even solids [3]. Images taken in scattering media are characterized by loss of contrast. Light passing through undergoes absorption and scattering, causing changes in color and brightness. Moreover, light that is scattered back from the medium along the light of sight (*backscatter*) veils the object, degrading the contrast. Therefore, applying traditional computer vision methods in such environments is difficult. Nevertheless, there is a strong need to perform vision tasks in these media. Examples include vision through biological tissue [16], underwater applications, such as port inspection, measuring ecological systems [15], and navigation in bad weather [1].

Previous studies tackled this challenge in various ways. Some recovered visibility as well as the 3D structure in haze and underwater [38], [39], [40] under distant natural illumination. However, application fields operating in highly turbid media use *artificial illumination* sources at *short* distances, be it underwater or in the human body. However, artificial lighting usually causes a strong *backscatter*. Backscatter can be modulated and then compensated for in image postprocessing. Prior modulation methods require acquisition of long image sequences by structured light [21], [23], [31] or time-gating [6], [9], [14], [47], [49]. Nayar et al. [32] required many frames as well, to achieve

quality results. Such sequences may lengthen the overall acquisition time. Moreover, such systems may be complex and expensive.

To counter these problems, we look at wide-field (not scanning) illumination with a small (or no) baseline, where the backscatter is modulated by polarization. Preliminary studies [10], [11], [24] indicated that backscatter can be reduced by polarization. However, we go further. By postprocessing, we remove residual backscatter that is not blocked by optical means. Moreover, a rough estimate of the 3D scene structure may be obtained from the acquired frames. The acquisition setup is a simple modification of instruments used routinely in such media: simply mounting two polarizers, one on the light source and another on the camera. The acquisition process is instantaneous, i.e., requiring only two frames, rather than scanning. In this paper, we describe and demonstrate each step separately.

Some prior methods used polarization in scattering media. Some assumed a negligible degree of polarization (DOP) of the objects [38], [39], [41], [50]. Others assumed the contrary, i.e., the object reflection is significantly polarized rather than the backscatter [52]. However, here we allow both the backscatter and the object reflection to be partially polarized. Thus, our analysis unifies and generalizes the mentioned previous methods.

The approach is based on several insights into the image formation process. We show that backscatter and attenuation of artificial illumination can be well approximated by simple closed-form parametric expressions. To incorporate polarization, we made some empirical observations in real underwater scenes: in a temperate latitude sea (the Mediterranean), in a tropical sea (the Red Sea), and in a murky lake (Sea of Galilee). Our approach has limits stemming from the wide-field nature of the illumination and from the acquisition noise. In this paper, we thoroughly

- The authors are with the Electrical Engineering Department, Technion-Israel Institute of Technology, Haifa 3200, Israel.
E-mail: ttali@tx.technion.ac.il, yoav@ee.technion.ac.il.

Manuscript received 3 Sept. 2007; revised 4 Feb. 2008; accepted 25 Feb. 2008; published online 1 Apr. 2008.

Recommended for acceptance by Y. Sato.

For information on obtaining reprints of this article, please send e-mail to: tpami@computer.org, and reference IEEECS Log Number TPAMI-2007-09-0547.

Digital Object Identifier no. 10.1109/TPAMI.2008.85.

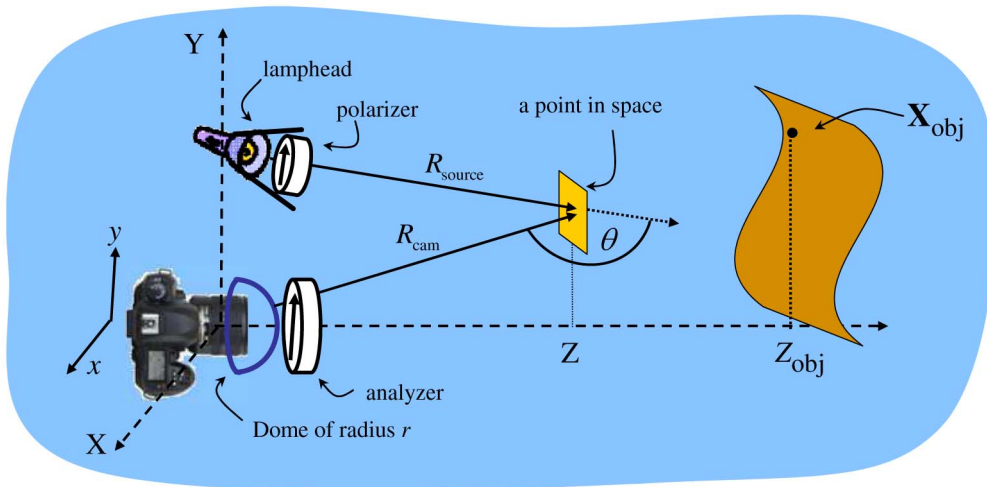


Fig. 1. A camera inside a dome port with a radius r . The variables are detailed in the text.

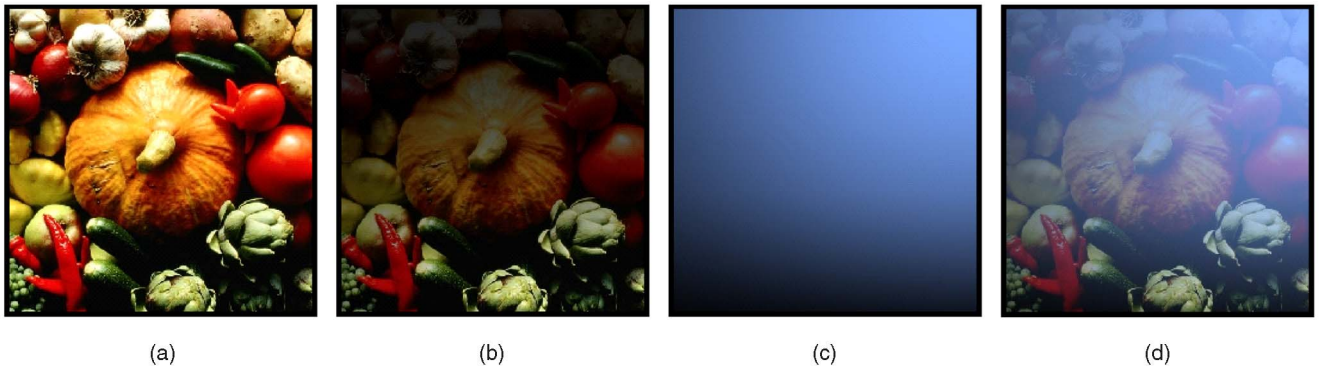


Fig. 2. Simulation of an underwater scene. The scene was assigned a linearly varying distance map ranging between $[0.2 \text{ m}, 1 \text{ m}]$. (a) A uniformly lit clear scene. (b) The simulated attenuated signal. (c) The backscatter component. (d) The sensed underwater scene, accounting for both scattering and attenuation.

analyze the reconstruction limits of both signal and 3D structure.

In Section 2, this paper first describes the scientific model of the imaging system and sets the ground for polarization imaging (Section 3). The reconstruction is done in two steps: First, we recover the object signal (Section 4). Then, we estimate the scene structure (Section 5). Experimental results follow each step. In Section 6, we discuss estimation of essential parameters. Then, Section 7 analyzes the limits of our method due to image noise. Partial results appeared in [50].

2 STATEMENT OF THE PROBLEM

Consider a perspective underwater camera (Fig. 1). Let $\mathbf{X} = (X, Y, Z)$ be the world coordinates of a point in the water. We set the world system's axes (X, Y) to be parallel to the (x, y) coordinates at the image plane, while Z aligns with the camera's optical axis, and the system's origin is at the camera's center of projection. The projection of \mathbf{X} on the image plane is $\mathbf{x} = (x, y)$. In particular, an object point at \mathbf{X}_{obj} corresponds to an image point \mathbf{x}_{obj} . The line of sight (LOS) to the object is

$$\text{LOS} \equiv \{\mathbf{X} : Z \in [0, Z_{\text{obj}}], X = (Z/f)x_{\text{obj}}, Y = (Z/f)y_{\text{obj}}\}, \quad (1)$$

where f is the camera's focal length. The measured image is

$$I(\mathbf{x}_{\text{obj}}) = S(\mathbf{x}_{\text{obj}}) + B(\mathbf{x}_{\text{obj}}), \quad (2)$$

where $S(\mathbf{x}_{\text{obj}})$ is the object signal and $B(\mathbf{x}_{\text{obj}})$ is the backscatter [17], [26], [28]. Before detailing these components, note that backscatter is the major cause of contrast deterioration [18] rather than signal blur. This was demonstrated in [38] and [39], using objective criteria. Interestingly, according to Wells [53], human vision associates image quality mostly with contrast rather than resolution. For these reasons, we do not focus here on image blur or deblurring. Rather, we consider the prime effects associated with turbidity to be backscatter and attenuation. Fig. 2 demonstrates these effects.

Define $L_{\text{obj}}(\mathbf{x}_{\text{obj}})$ as the object radiance we would have sensed had no disturbances been caused by the medium along the LOS and under uniform illumination. Propagation of light to the object and then to the camera via the medium yields an attenuated [17], [26] signal. The signal is



Fig. 3. An example of an anisotropic illumination pattern $Q(\mathbf{X})$: Even in the same radial distance from the lamphead, the lighting changes laterally.

$$S(\mathbf{x}_{\text{obj}}) = L_{\text{obj}}(\mathbf{x}_{\text{obj}})F(\mathbf{x}_{\text{obj}}), \quad (3)$$

where F is a falloff function described below.

A point \mathbf{X} in the water is at total distance $\|\mathbf{X}\|$ from the camera. If the camera is enclosed in a dome port¹ as in [38], [39], then the distance from the dome to \mathbf{X} is

$$R_{\text{cam}}(\mathbf{X}) = \|\mathbf{X}\| - r, \quad (4)$$

where r is the dome's radius. Consider for a moment a single illumination point source. From this source, light propagates a distance R_{source} to \mathbf{X}_{obj} . Free space propagation creates a $1/R_{\text{source}}^2$ irradiance falloff. Yet, there is turbidity, characterized by an attenuation coefficient c . Hence,

$$F(\mathbf{x}_{\text{obj}}) = \frac{\exp\{-c[R_{\text{source}}(\mathbf{X}_{\text{obj}}) + \|\mathbf{X}_{\text{obj}}\| - r]\}}{R_{\text{source}}^2(\mathbf{X}_{\text{obj}})} Q(\mathbf{X}_{\text{obj}}). \quad (5)$$

Here, $Q(\mathbf{X})$ expresses the nonuniformity of the scene irradiance (Fig. 3), solely due to the angular inhomogeneity of the illumination (anisotropy), which is insensitive to the medium properties. Thus, in water-based media, for example, it can be precalibrated in clear water. For multiple illumination sources, or for a wide spread source, (5) is derived for each point source, and then all F 's are summed up. This can be generalized to include illumination due to multiple scattering [48].

In order to calculate the backscatter that appears in (2), first define I^{source} as the irradiance of a point in the volume [17] by a small illumination source of intensity L^{source} :

$$I^{\text{source}}(\mathbf{X}) = L^{\text{source}} [1/R_{\text{source}}^2(\mathbf{X})] \exp[-cR_{\text{source}}(\mathbf{X})] Q(\mathbf{X}). \quad (6)$$

Then, according to the single scattering model (Fig. 4), the backscatter is given [17], [50] by integration along the LOS:

$$B(\mathbf{x}_{\text{obj}}) = \int_{R_{\text{cam}}=0}^{R_{\text{cam}}(\mathbf{x}_{\text{obj}})} b[\theta(\mathbf{X})] I^{\text{source}}(\mathbf{X}) \exp[-cR_{\text{cam}}(\mathbf{X})] dR_{\text{cam}}, \quad \mathbf{X} \in \text{LOS}, \quad (7)$$

where $\theta \in [0, \pi]$ is the scattering angle, and b is the scattering coefficient² of the medium: It expresses the ability of an

1. Dome ports often shield cameras from water [38], [39]. With a dome, optical distortions are smaller than when using other shapes of windows, provided that the center of projection of the lens is accurately aligned with the center of the dome. Schechner and Karpel [38], [39] explain that when the lens and the dome are aligned, the polarization measurement is more accurate because chief light rays do not change their path when passing through the port. Distortions caused by a flat port are analyzed and calibrated in [51].

2. Note that $b(\theta)$ and c depend on the wavelength. Thus, each available wavelength band is analyzed independently.

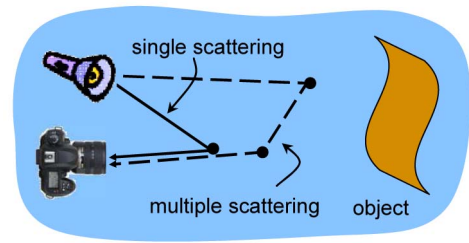


Fig. 4. Backscatter caused by single scattering (solid line) and multiple scattering (dashed).

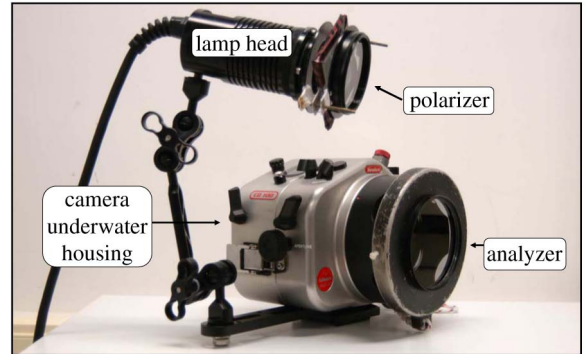


Fig. 5. A single lamphead version of our system.

infinitesimal medium volume to scatter flux to θ . Equation (7) applies to each illumination source: Accumulating the results yields the total backscatter. Note that the integration in (7) stops when it reaches the object in the LOS. Therefore, the backscatter accumulates (increases) with the object distance. If there is no object on the LOS, the integration in (7) continues to an infinite distance. The value of B then increases until it reaches a *saturation value*. We term the distance in which B effectively saturates³ as the *saturation distance* z_{sat} .

Our goal in this research is twofold: First is to estimate the backscatter component, in order to remove it from the raw image and reveal the object signal. Second is to study the potential use of the backscatter component for extracting information about the distance map of the scene. Section 3 describes how we achieve the first goal by polarizing the light source.

3 POLARIZATION IMAGING

As mentioned earlier, we suggest modulating the light by polarizing the light source and imaging through a camera-mounted polarizer (*analyzer*) in two orthogonal polarization states. The system setup is depicted in Figs. 1 and 5. By mounting a polarizer (either linear or circular) on the light source, we polarize the illumination. The polarized light propagates to illuminate the scene and part of it is scattered back by particles in the medium toward the camera. During this propagation, some energy of the light becomes unpolarized (a process termed *depolarization*). This process

3. As in every asymptotic function, the effective distance can be defined in different ways. For example, it can be defined as the distance where B reaches 99 percent of its maximum value.

is complex and depends on the distribution of particle types and sizes [19], [25], [36]. Apparently, this process affects each polarization type differently: Some studies suggest that depolarization during propagation is weaker in circular polarization [19], [25], [29], [36], while Jarry et al. [19] and Sankaran et al. [36] suggest weaker depolarization of linear polarization in dense tissues. An empirical study [44] has looked at the rate of depolarization with distance in seawater. A preliminary empirical study [11] done decades ago has shown that if the illumination is circularly polarized, then it flips handedness upon backscattering. Thus, Gilbert and Pernicka [11] achieved significant improvement in image contrast in an optical method, where it used an analyzer having the same handedness as the illumination polarizer.

That said, despite the scientific efforts that have been invested by various researchers (see, for example, [33]), the known art has not supplied a clear answer as to which polarization type is preferable in the true environments we worked in and how the depolarization rate can be determined by the scattering and attenuation coefficients in those environments. Therefore, we tested our method with either linear or circular polarization in different locations. In the case of linear polarization, we mount a linear polarizer on the light source and a linear analyzer on the camera. Then, an orthogonal image pair is taken by either rotating the polarizer or the analyzer. Specifically, we chose to rotate the analyzer as it was easier in our setup. When using circular polarization, orthogonal states result from switching handedness rather than rotating the polarizers. As a consequence, linear polarization is easier to use. Moreover, wideband and wide-field circular polarization is difficult to create. In any case, raw polarized data still contains significant backscatter. Therefore, there is a need for postprocessing, as described in Section 4. The postprocessing we perform does not depend on the polarization type used.

4 BACKSCATTER REMOVAL BY POLARIZATION

This section describes and demonstrates through experiments visibility enhancement by active polarization imaging. This is done by separating the signal and the backscatter components. Later, in Section 5.1, we explain how the estimated backscatter may be used for estimating the 3D structure of the scene.

4.1 Model and Algorithm

Previous studies have used polarized illumination for backscatter removal. In [50], we assumed that objects backreflect unpolarized light to the camera. On the other hand, studies using polarization difference imaging (PDI) assume the opposite—that the light reflected from the objects is polarized and that the backscatter is almost unpolarized. Here, we give a more general model. Fortunately, if the object yields polarized specular reflection, it behaves similarly to the backscatter: Out of the two frames, generally the one in which the backscatter is brighter is also the one in which the object backreflection is brighter.⁴

As described in Section 3, we take two images of the same scene using two orthogonal polarization states of

the polarizer. Had the backscattered light completely retained its polarization, it could have been optically eliminated by the analyzer. We discovered that a substantial DOP is maintained upon backscattering. We exploit this phenomenon.⁵ Consequently, placing an analyzer in the orthogonal state to the backscatter's polarization state yields an image with minimum visible backscatter. We denote this image as I^{\min} . Imaging with the opposite orthogonal state, denoted as I^{\max} , maximizes the backscatter.

We expand (2) to the polarized components B_{\max} , B_{\min} , S_{\max} , and S_{\min} . Thus, the raw images are

$$\begin{aligned} I_{\max}(\mathbf{x}_{\text{obj}}) &= S_{\max}(\mathbf{x}_{\text{obj}}) + B_{\max}(\mathbf{x}_{\text{obj}}), \\ I_{\min}(\mathbf{x}_{\text{obj}}) &= S_{\min}(\mathbf{x}_{\text{obj}}) + B_{\min}(\mathbf{x}_{\text{obj}}). \end{aligned} \quad (8)$$

The DOP of the signal p_{obj} and the DOP of the backscatter p_{scat} are defined as

$$\begin{aligned} p_{\text{obj}}(\mathbf{x}_{\text{obj}}) &= \frac{S_{\max}(\mathbf{x}_{\text{obj}}) - S_{\min}(\mathbf{x}_{\text{obj}})}{S_{\max}(\mathbf{x}_{\text{obj}}) + S_{\min}(\mathbf{x}_{\text{obj}})}, \\ p_{\text{scat}}(\mathbf{x}_{\text{obj}}) &= \frac{B_{\max}(\mathbf{x}_{\text{obj}}) - B_{\min}(\mathbf{x}_{\text{obj}})}{B_{\max}(\mathbf{x}_{\text{obj}}) + B_{\min}(\mathbf{x}_{\text{obj}})}. \end{aligned} \quad (9)$$

In the following, \mathbf{x}_{obj} is omitted for simplicity. We end up with two equations for the two unknown fields S and B :

$$\mathbf{I}_{\max} + \mathbf{I}_{\min} = \mathbf{B} + \mathbf{S}, \quad (10)$$

$$\mathbf{I}_{\max} - \mathbf{I}_{\min} = p_{\text{scat}}\mathbf{B} + p_{\text{obj}}\mathbf{S}. \quad (11)$$

The last equation is derived from plugging (9) into (8). The solution to this equation set is

$$\hat{\mathbf{S}} = \frac{1}{p_{\text{scat}} - p_{\text{obj}}} [\mathbf{I}_{\min}(1 + p_{\text{scat}}) - \mathbf{I}_{\max}(1 - p_{\text{scat}})], \quad (12)$$

$$\hat{\mathbf{B}} = \frac{1}{p_{\text{scat}} - p_{\text{obj}}} [\mathbf{I}_{\max}(1 - p_{\text{obj}}) - \mathbf{I}_{\min}(1 + p_{\text{obj}})]. \quad (13)$$

This is a general result, enabling separation of \mathbf{B} and \mathbf{S} from the two raw images, given the DOPs p_{obj} and p_{scat} .

A very important property of (12) is that p_{obj} contributes only a scale factor to the signal reconstruction $\hat{\mathbf{S}}$. Suppose that p_{obj} is approximately constant across the scene, but it is unknown. Then, the signal estimation (12) is consistent with the true \mathbf{S} up to a scale. For purposes of visibility enhancement, the scaled $\hat{\mathbf{S}}$ is sufficient: The backscatter is removed and missing parts are revealed. Furthermore, the backscatter is usually not uniform across the image; some regions have high intensity backscatter and others have low intensity backscatter (see Fig. 2). This hampers standard image enhancement techniques. Therefore, removing the backscatter results in a signal estimation $\hat{\mathbf{S}}$ with a more uniform intensity. Thus, further image improvement may be obtained by applying standard image enhancement techniques to $\hat{\mathbf{S}}$, rather than applying them to \mathbf{I} or \mathbf{I}_{\min} .

As p_{obj} changes only the scale of \mathbf{S} , good results can be achieved [38], [39], [41], [50] based on the assumption that $p_{\text{obj}} = 0$. In this case, (12) and (13) reduce to

4. Empirically, we never encountered a reversed polarization of the signal relative to the backscatter.

5. Polarization has also aided other computer vision aspects [2], [5], [7], [8], [27], [40], [43], [45], [54].

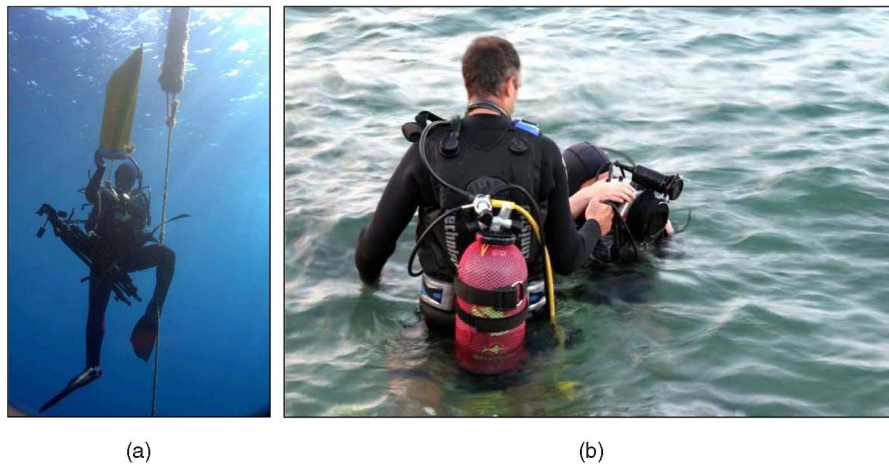


Fig. 6. (a) Scuba diving with a lift bag, toward night experiments in the Red Sea. (b) Preparations for an experiment in the Mediterranean.

$$\hat{\mathbf{S}} = [\mathbf{I}_{\min}(1 + p_{\text{scat}}) - \mathbf{I}_{\max}(1 - p_{\text{scat}})]/p_{\text{scat}}, \quad (14)$$

$$\hat{\mathbf{B}} = (\mathbf{I}_{\max} - \mathbf{I}_{\min})/p_{\text{scat}}. \quad (15)$$

Note that, in this case,

$$\mathbf{I}_{\min} = [\mathbf{B}(1 - p_{\text{scat}}) + \mathbf{S}]/2, \mathbf{I}_{\max} = [\mathbf{B}(1 + p_{\text{scat}}) + \mathbf{S}]/2. \quad (16)$$

Let us examine the consequence of using an assumption $p_{\text{obj}} = 0$ in (13), when image creation (8) experienced $p_{\text{obj}} \neq 0$. This case yields a false estimation $\tilde{\mathbf{B}}$ of the backscatter:

$$\tilde{\mathbf{B}} = \frac{\mathbf{I}_{\max} - \mathbf{I}_{\min}}{p_{\text{scat}}} = \hat{\mathbf{B}} + \frac{\mathbf{S}_{\max} - \mathbf{S}_{\min}}{p_{\text{scat}}} = \hat{\mathbf{B}} + \frac{p_{\text{obj}}}{p_{\text{scat}}} \mathbf{S}. \quad (17)$$

The last equality results from plugging in the DOP p_{obj} from (9). As discussed in Section 2, \mathbf{B} increases with the distance. From (5), when the camera and the light sources are on the same side of the object (a common scenario), \mathbf{S} decreases with the distance. In that case, a result of (17) is that $\tilde{\mathbf{B}}$ is no longer monotonic with Z_{obj} .

As opposed to the assumption $p_{\text{obj}} = 0$, methods based on PDI [52] assume that $p_{\text{scat}}/p_{\text{obj}} \rightarrow 0$. Plugging $p_{\text{scat}}/p_{\text{obj}} \rightarrow 0$ to (12) and (13) results in

$$\hat{\mathbf{S}} = \frac{1}{p_{\text{obj}}} [\mathbf{I}_{\max} - \mathbf{I}_{\min}], \quad (18)$$

$$\hat{\mathbf{B}} = \frac{1}{p_{\text{obj}}} [\mathbf{I}_{\min}(1 + p_{\text{obj}}) - \mathbf{I}_{\max}(1 - p_{\text{obj}})]. \quad (19)$$

Note that, in this case, (18) is a scaled version of the polarization difference image. Here, we see that (12) and (13) unify both the dehazing methods [38], [39], [41], [50], where $p_{\text{obj}} = 0$, and the PDI methods where $p_{\text{scat}}/p_{\text{obj}} \rightarrow 0$.

Using (12) and (13) without such approximations requires the estimation of the DOPs. Section 6 describes how the DOPs are estimated in the general case. First, however, we demonstrate backscatter removal in experiments.

4.2 Experiments

The method described above is general and it does not assume a specific medium. However, as discussed in

Section 3, depolarization depends on the medium [22]. Therefore, in order to demonstrate the effectiveness of the method in real-world situations, we embarked on underwater dives rather than using indoor tanks. Particles in substances (like milk, lipids, etc.) used for diluting water in indoor tanks are usually homogeneous and sometimes symmetric [19], [35], while oceanic particles are heterogeneous [28]. Therefore, we were concerned that polarization experiments done with diluted substances would not represent correctly the properties and the variety of the media in the field, e.g., seawater. We have done experiments while scuba diving at night in various environments, in a pool, the Red Sea, the Mediterranean (Fig. 6), and the Sea of Galilee.

4.3 Equipment

Fig. 5 shows that the system we used has two main parts:

- An SLR camera with an underwater housing. We use a Nikon D100 camera, which has a linear response [38], [39]. The camera is placed in a Sealux underwater housing with a mounted polarizer. The considerations for choosing a camera, an underwater housing, and mounted polarizers are detailed in [38], [39].
- Underwater AquaVideo light sources, with 80 W halogen bulbs. A polarizer is mounted on the lighthead. We had special consideration behind the selection of the lighting setup, as detailed in the Appendix.

We used standard off-the-shelf polarizers of Schneider and Tiffen. The camera was mounted on a tripod. To safely transport this amount of equipment while diving, a 50-kg lift bag was used (Fig. 6). The tripod was set to resist swell by attaching weights on its lower part.

4.4 Real-World Results

Fig. 7 shows the results of applying (14) and (15) on images taken during four different experiments we have performed. We tested the method using different light source locations. The left column presents the raw images \mathbf{I} . The center column shows $\hat{\mathbf{S}}$ (where the estimated backscatter is removed). The right column shows the estimated backscatter

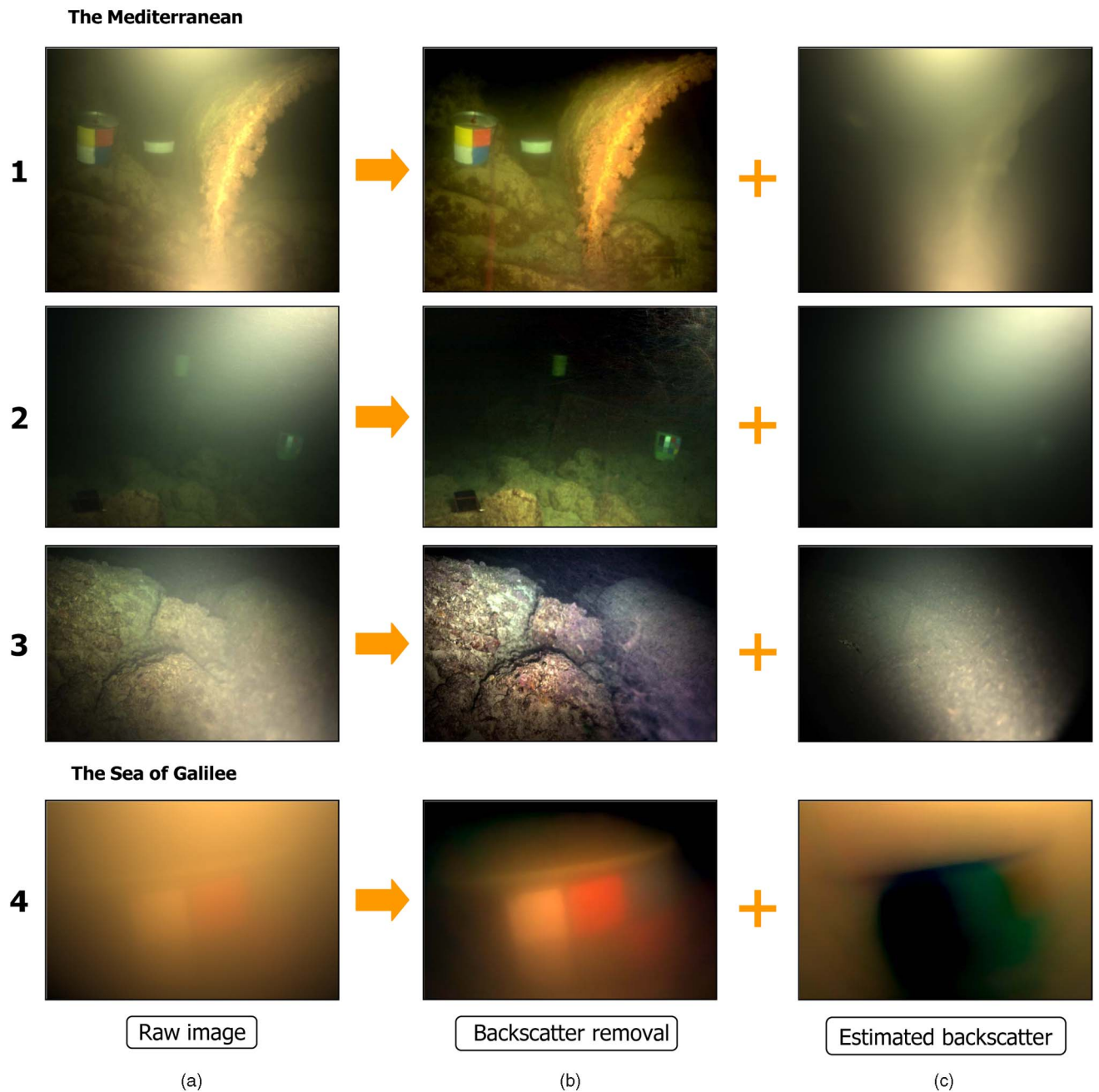


Fig. 7. Results of four different experiments. (a) The raw images I . (b) The recovered signals \hat{S} (backscatter removal). (c) The estimated backscatter fields \hat{B} .

component \hat{B} . The experiments in the three top rows were performed in the Mediterranean on three different occasions. In all three cases, using linear polarizers have yielded a DOP of $p_{\text{scat}} \approx 65\%$. In **experiment 1**, we used two light sources, shining from above and below the camera. Here, $Z_{\text{obj}} < 3$ m. Notice the revealed rock in the upper left part, the sand in the right side, the rocks on the bottom, and the distant part of the tube. In **experiment 2**, $Z_{\text{obj}} \in [0.5 \text{ m}, 6 \text{ m}]$. Here, we used a single light source, coming from the top right. Notice the revealed rectangular cube in the background. The revealed objects in the background are dark, as at this distance they receive only dim irradiance from the sources. **Experiment 3** shows a scene illuminated from the bottom

right. Consequently, the lower parts have a lot of backscatter and, hence, poor visibility. Our method enhanced the visibility in this part.

Experiment 4 shows a result of an experiment done in the Sea of Galilee, a very murky lake. The light source is placed above the camera. Here, $Z_{\text{obj}} \approx 0.5$ m, which was the maximum visibility distance. Here, circular polarization yielded $p_{\text{scat}} \approx 9$ percent while linear polarization yielded $p_{\text{scat}} \approx 5$ percent. Despite the difficult conditions, the method revealed the imaged object, its rough contour, and its colors. Notice that, in both **experiments 2** and **4**, the upper part of the raw frame is very bright, due to backscatter. This may cause the viewer to falsely assume that there is a bright

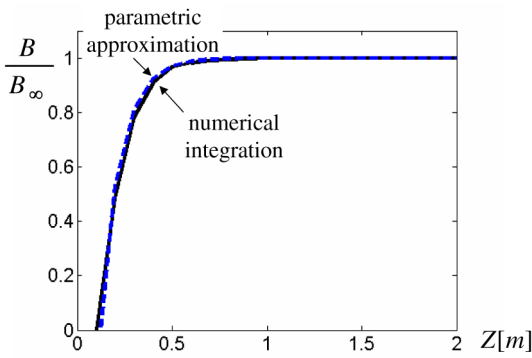


Fig. 8. The backscatter given by (7) as approximated by (21), with $c = 0.1 \text{ m}^{-1}$.

object in that part of the scene. After removal of the backscatter, these areas become dark as there is actually no light reflecting from objects there. Then, we expect the scene radiance to act according to (5). Indeed, in **experiment 2**, the brightest part of $\hat{\mathbf{S}}$ is the lower, close sand.

In our field experiments, both polarization types (linear and circular) yielded good results. When visibility was moderate (in the Mediterranean), linear polarization retained $p_{\text{scat}} \approx 60\text{-}70\%$, higher than circular polarization, for which $p_{\text{scat}} \approx 50\%$. In the murky Sea of Galilee, on the other hand, circular DOP was higher than the linear one. There, perceptual difference hardly existed between the raw frames, due to the low DOP value. Nevertheless, our method still enhanced $\hat{\mathbf{S}}$ significantly.

5 RANGE AND FALLOFF

5.1 Range

Let us have an estimate for the backscatter $\hat{\mathbf{B}}$ in a scene, for example, using the method in Section 4. We would like to know if we may leverage $\hat{\mathbf{B}}$ to estimate the 3D structure of the scene. A general approach is presented for estimating Z_{obj} based on $\hat{\mathbf{B}}$. It does not depend on the algorithm used for extracting $\hat{\mathbf{B}}$ itself.

Similarly to [4], [30], [38], [39], [41], the backscatter B increases with the distance Z_{obj} ; hence, it can indicate the distance. Previously [38], [39], [41], this principle was developed in the simple special case of distant illumination sources (natural light), where the following relation holds:

$$\begin{aligned} B &= B_{\infty} \{1 - \exp[-cR_{\text{cam}}(x, y, Z_{\text{obj}})]\} \\ &\approx B_{\infty} \{1 - \exp[-cZ_{\text{obj}}(x, y)]\}. \end{aligned} \quad (20)$$

Such an estimation can be generalized to the use of sources close to the camera. We found numerically [50] that in wide-field lighting, (7) can be approximated as

$$\begin{aligned} B(\mathbf{x}_{\text{obj}}) &\approx B_{\infty}(\mathbf{x}_{\text{obj}}) \cdot \\ &(1 - \exp[-\{-k(\mathbf{x}_{\text{obj}})[Z_{\text{obj}}(\mathbf{x}_{\text{obj}}) - Z_0(\mathbf{x}_{\text{obj}})]\}]), \end{aligned} \quad (21)$$

resembling (20). Fig. 8 presents an approximation done for a particular setup. A major difference between (20) and (21) is that in (21) B_{∞} is space variant. Equation (21) introduces two new space-variant parameters, $Z_0(\mathbf{x}_{\text{obj}})$ and $k(\mathbf{x}_{\text{obj}})$. The offset Z_0 is a distance, which indicates the first effective intersection of the LOS with the light cone emitted by the lamphed. The

rate at which B increases with Z_{obj} at Z_0 is set by k . These parameters (B_{∞}, Z_0, k) depend on the lighting geometry, the nonuniformity (anisotropy) $Q(\mathbf{X}_{\text{obj}})$ of the illumination sources and on the medium parameters c and b (described in Section 2). They do *not* depend on Z_{obj} .

Equation (21) is easy to invert, deriving an estimate $\hat{Z}_{\text{obj}}(\mathbf{x}_{\text{obj}})$ as a function of $\hat{B}(\mathbf{x}_{\text{obj}})$:

$$\hat{Z}_{\text{obj}}(\mathbf{x}_{\text{obj}}) = Z_0(\mathbf{x}_{\text{obj}}) - \left[\ln \left(1 - \frac{\hat{B}(\mathbf{x}_{\text{obj}})}{B_{\infty}(\mathbf{x}_{\text{obj}})} \right) \right] \frac{1}{k(\mathbf{x}_{\text{obj}})}. \quad (22)$$

This, of course, requires calibration of the spatially varying parameter fields B_{∞} , k , and Z_0 . An important parameter is B_{∞} . It expresses the backscatter at \mathbf{x}_{obj} had there been no object in the LOS. Therefore, the relation

$$B_{\text{rel}}(\mathbf{x}_{\text{obj}}) = \frac{\hat{B}(\mathbf{x}_{\text{obj}})}{B_{\infty}(\mathbf{x}_{\text{obj}})} \quad (23)$$

indicates how much the backscatter has reached its saturation value B_{∞} . Thus, B_{rel} is monotonic with Z_{obj} . The parameters k and Z_0 function as scaling factors in (22). It is easy [50] to determine the field B_{∞} by taking a photograph in the medium, where the camera is pointing “nowhere” (to infinity). By approximating k and Z_0 to be uniform and plugging in typical values for them in (22), a rough distance map can be estimated.

We simulated similar setups to those we used in our experiments. To simplify the analysis, let us assume that the backscatter coefficient $b(\theta)$ is uniform in the range of angles we use. This assumption is supported by [22], which shows that in oceanic water the function $b(\theta)$ is insensitive to θ at backscatter angles ($\theta \geq \pi/2$). Fig. 9 shows a distance map derived by applying (22) and (23) on an underwater scene. For (22), we used the values $Z_0 = 20 \text{ cm}$ and $k = 0.6$. Those values were chosen based on a numerical analysis of setups where the light source was in proximity to the camera. This analysis showed that Z_0 ranges between 10 and 30 cm and k ranges between 3 and 6. The value of k changes between different illumination camera setups. It also changes spatially in the image, pixels closer to the light source having a higher k .

5.2 Falloff

Section 5.1 described the estimation of $\hat{Z}_{\text{obj}}(\mathbf{x}_{\text{obj}})$. Based on $\hat{Z}_{\text{obj}}(\mathbf{x}_{\text{obj}})$, we may now estimate the falloff, using (5). Here, we need three additional parameters. First is the attenuation coefficient c , which can be measured by a transmissiometer. Second, we need $Q(\mathbf{X}_{\text{obj}})$. This can be precalibrated once per light source. In addition, there is a need to know R_{source} . It is derived based on a priori knowledge about the system baseline [48]: It is sufficient to know the camera-light-source baseline R_{sc} and the angle between this source and the LOS, γ (see Fig. 1). Then,

$$R_{\text{source}} = \sqrt{R_{\text{sc}}^2 + R_{\text{cam}}^2 - 2R_{\text{cam}}R_{\text{sc}} \cos \gamma}. \quad (24)$$

The value of \hat{R}_{cam} is estimated by setting $z = \hat{Z}_{\text{obj}}$ in (4). Then, (24) derives \hat{R}_{source} . The use of \hat{Z}_{obj} and \hat{R}_{source} in (5) derives an estimate for the falloff $\hat{F}(\mathbf{x}_{\text{obj}})$. Compensating for the falloff by inverting (3) yields

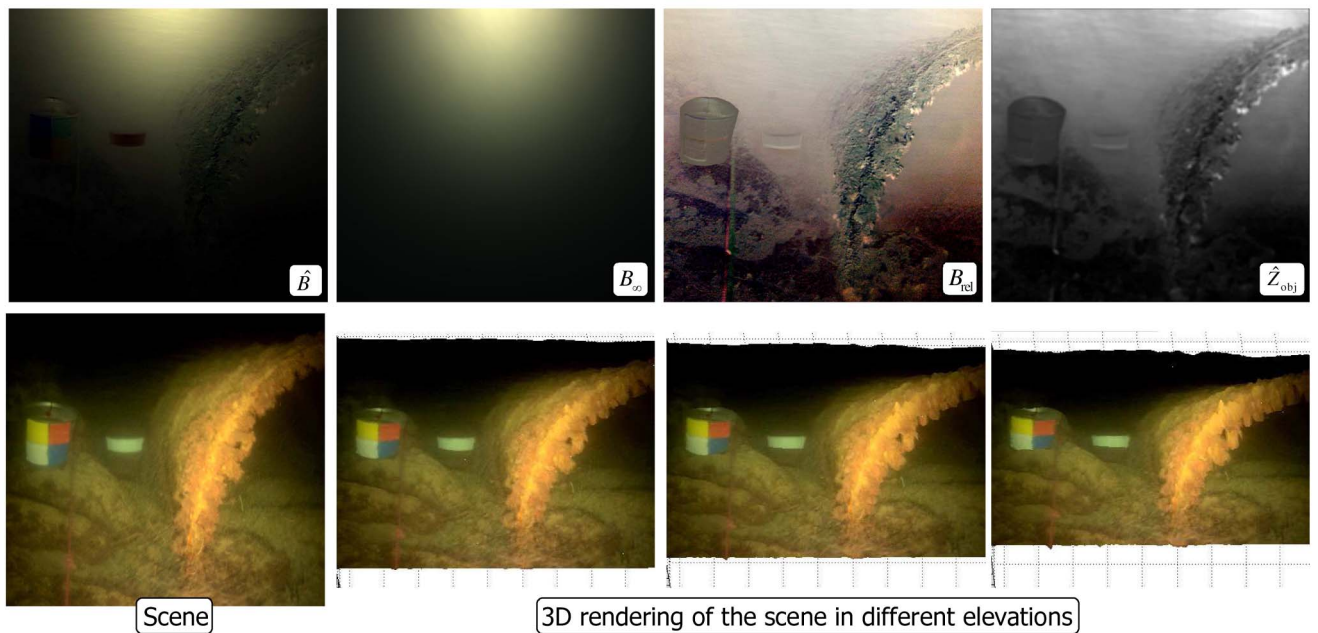


Fig. 9. Estimation of a distance map. (a) The different components of (21) and (23) in an underwater experiment. The image B_{rel} is scaled to yield an estimation of the distance map. (b) Views from different elevations of the reconstructed 3D scene composed of the recovered signal and the estimated distance map.

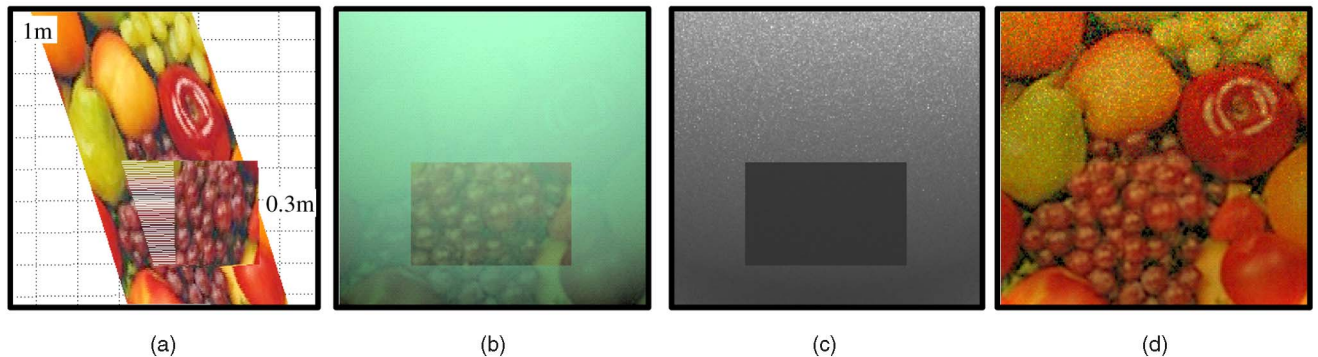


Fig. 10. Simulated backscatter removal, 3D recovery, and falloff compensation of a noisy object. (a) An object was assigned a distance map varying linearly to 1 m with a sticking rectangle at a distance of 0.3 m. (b) The simulated underwater raw frame I , with added noise. (c) The estimated distance map \hat{Z}_{obj} . (d) The recovered object radiance \hat{L}_{obj} . In (c) and (d), the noise is amplified in the distant parts.

$$\hat{L}_{object}(\mathbf{x}_{obj}) = \hat{S}(\mathbf{x}_{obj}) / \hat{F}(\mathbf{x}_{obj}). \quad (25)$$

To illustrate this, Fig. 10 shows a simulation of the entire recovery method. A simulated object was assigned a nontrivial distance map and artificial noise was added with standard deviation (STD) of $\sigma_{I_{min}} = \sigma_{I_{max}} = 1$ gray level (out of 256 gray levels in the raw frames I_{min}, I_{max}). Fig. 10d shows $\hat{L}_{object}(\mathbf{x}_{obj})$ after both removal of the estimated backscatter and falloff compensation. While the image is enhanced relative to the simulated I , there is noise amplification in the distant parts [20], [37].

6 ESTIMATION OF THE DOPS

In Section 4, we use the parameters p_{scat} and p_{obj} to reconstruct S and B . Ways for estimating these parameters are discussed now.

6.1 Extraction of p_{scat}

Light depolarizes as it propagates [44]. Therefore, it is reasonable to expect the measured p_{scat} to be nonuniform. The reason for this is that backscattered light from a large Z_{obj} contributes p_{scat} that is smaller than light backscattered from a small Z_{obj} . In total, the measured p_{scat} is influenced by light that is backscattered from all distances (up to the object), close and far, on the LOS. However, we found empirically that the value of p_{scat} is practically constant across the field of view (FOV) in seawater.⁶ A possible explanation to this phenomenon is demonstrated in Figs. 8 and 16: After a short distance, the backscatter is saturated. Therefore, backscatter stemming from large distances (with a low p_{scat}) has almost no influence on the measurement.

As p_{scat} is practically uniform, it is easy to measure. It can be retrieved in several distinct ways. These include:

6. We found it is constant up to ≈ 24 degrees relative to the optical axis.

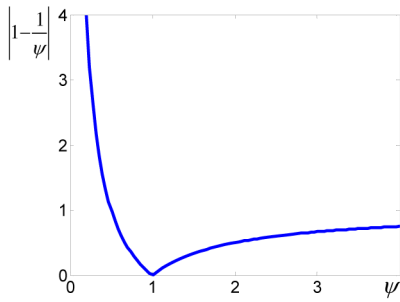


Fig. 11. Influence of a wrongly estimated p_{scat} . The relative error is typically smaller in overestimation of p_{scat} than in underestimation.

1. Measuring an area \mathbf{x}_{void} in the FOV in which there is no signal. Since there is no object in \mathbf{x}_{void} , then $\mathbf{I}_{\text{max}}(\mathbf{x}_{\text{void}}) = \mathbf{B}_{\text{max}}(\mathbf{x}_{\text{void}})$ and $\mathbf{I}_{\text{min}}(\mathbf{x}_{\text{void}}) = \mathbf{B}_{\text{min}}(\mathbf{x}_{\text{void}})$. Thus,

$$\hat{p}_{\text{scat}}(\mathbf{x}_{\text{void}}) = \frac{I_{\text{max}}(\mathbf{x}_{\text{void}}) - I_{\text{min}}(\mathbf{x}_{\text{void}})}{I_{\text{max}}(\mathbf{x}_{\text{void}}) + I_{\text{min}}(\mathbf{x}_{\text{void}})}. \quad (26)$$

Assuming that p_{scat} is uniform across the scene, (26) yields an estimation of p_{scat} for the entire FOV.

2. Rigidly shifting the camera/illuminator system, to point to a void region in the medium (where no object is in sight), as in Section 5.1. Then, an image pair $\mathbf{I}_{\text{max}}, \mathbf{I}_{\text{min}}$ is acquired. In this case, every pixel points to a void. Therefore, using this pair with (26) yields a potentially spatially varying p_{scat} . This method enables a more flexible model.

Let us analyze the consequences of a mistake in the estimation of p_{scat} , i.e.,

$$\hat{p}_{\text{scat}} = \psi p_{\text{scat}}^{\text{true}}, \quad (27)$$

where $p_{\text{scat}}^{\text{true}}$ is the true backscatter DOP. Underestimation and overestimation correspond to $\psi < 1$ and $\psi > 1$, respectively. If $p_{\text{obj}} = 0$, then using (27) in (15) yields an erroneous estimate:

$$\tilde{\mathbf{B}} = \frac{\mathbf{I}_{\text{max}} - \mathbf{I}_{\text{min}}}{\psi p_{\text{scat}}^{\text{true}}} = \frac{1}{\psi} \mathbf{B}. \quad (28)$$

Similarly, the signal is erroneously estimated as

$$\tilde{\mathbf{S}} = \mathbf{I} - \frac{1}{\psi} \mathbf{B} = \mathbf{S} + \left(1 - \frac{1}{\psi}\right) \mathbf{B}. \quad (29)$$

The relative backscatter error

$$\mathbf{E}_B^{\text{rel}} = \left| \frac{\tilde{\mathbf{B}} - \mathbf{B}}{\mathbf{B}} \right| = |1/\psi - 1| \quad (30)$$

is constant over the FOV. On the other hand,

$$\mathbf{E}_S^{\text{rel}} = \left| \frac{\tilde{\mathbf{S}} - \mathbf{S}}{\mathbf{S}} \right| = |1/\psi - 1| \frac{B(\mathbf{x}_{\text{obj}})}{S(\mathbf{x}_{\text{obj}})} \quad (31)$$

depends on $B(\mathbf{x}_{\text{obj}})/S(\mathbf{x}_{\text{obj}})$. Generally, B/S increases with Z_{obj} ; hence, $\tilde{\mathbf{S}}$ is more affected by this error. Fig. 11 depicts $|1/\psi - 1|$, which is the part that depends on ψ in $\mathbf{E}_B^{\text{rel}}$ and

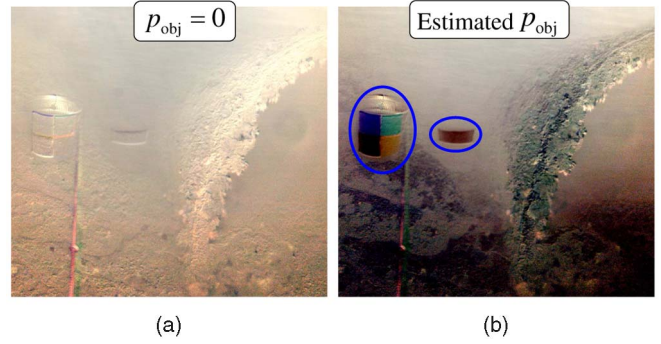


Fig. 12. An image of $\hat{\mathbf{B}}_{\text{rel}}$ in an underwater scene. (a) When assuming $p_{\text{obj}} = 0$, areas in proximity to the camera (lower part of the image) are falsely assigned a high value. (b) Using an estimated p_{obj} reveals that $\hat{\mathbf{B}}_{\text{rel}}$ is indeed low at close distances. Here, p_{obj} is assumed to be spatially uniform. Areas that do not comply with this assumption stand out (blue ellipses).

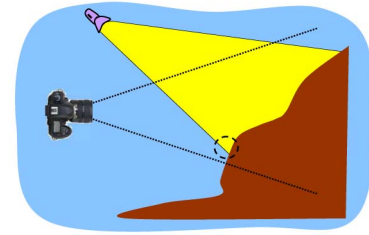


Fig. 13. Off-axis illumination results in areas with low backscatter (the circled part). This area can be sampled to estimate \hat{p}_{obj} .

$\mathbf{E}_S^{\text{rel}}$. From Fig. 11, the relative error is typically smaller when $\psi > 1$. Therefore, it is better to overestimate p_{scat} rather than underestimating it.

6.2 Estimating p_{obj}

Section 4 shows that, for purposes of signal reconstruction, it is possible to assume that $p_{\text{obj}} = 0$. However, from (13), if this assumption is wrong, it damages the estimation of $\hat{\mathbf{B}}$. As a consequence, it damages the estimation of the object distances Z_{obj} , based on $\hat{\mathbf{B}}$, as described in Section 5.1. Failing to estimate p_{obj} correctly damages the monotonic relation between $\hat{\mathbf{B}}$ and Z_{obj} expressed in (21). For illustration, in a real scene that we present in the following, $p_{\text{obj}} \approx 30\%$ at the rocks. In Fig. 12a, $\hat{\mathbf{B}}_{\text{rel}}$ is estimated under the wrong assumption that $\hat{p}_{\text{obj}} = 0$. Here, $\hat{\mathbf{B}}_{\text{rel}}$ is rather uniform, despite variations of Z_{obj} . On the other hand, when taking into consideration $p_{\text{obj}} \approx 30\%$, Fig. 12b reveals the significant dependency of $\hat{\mathbf{B}}_{\text{rel}}$ on Z_{obj} in this case.

Sometimes p_{obj} can be sampled directly from the images. Consider the marked circle in Fig. 13; in off-axis illumination, the objects at the far fringe of the irradiated spot are lit but are effectively not veiled by backscatter (as in [31]).

In Fig. 14a, for example, this occurs in the upper left part of the FOV. Term such an image location as $\mathbf{x}_{\text{clear}}$. In such areas, $\mathbf{I}_{\text{max}} \approx \mathbf{S}_{\text{max}}$ and $\mathbf{I}_{\text{min}} \approx \mathbf{S}_{\text{min}}$. Then, similarly to (26),

$$\hat{p}_{\text{obj}} = \frac{I_{\text{max}}(\mathbf{x}_{\text{clear}}) - I_{\text{min}}(\mathbf{x}_{\text{clear}})}{I_{\text{max}}(\mathbf{x}_{\text{clear}}) + I_{\text{min}}(\mathbf{x}_{\text{clear}})}. \quad (32)$$

For example, in the scene presented in Fig. 14, the measured values of \hat{p}_{obj} in the red, green, and blue channels are 0.22, 0.27, and 0.34, respectively.

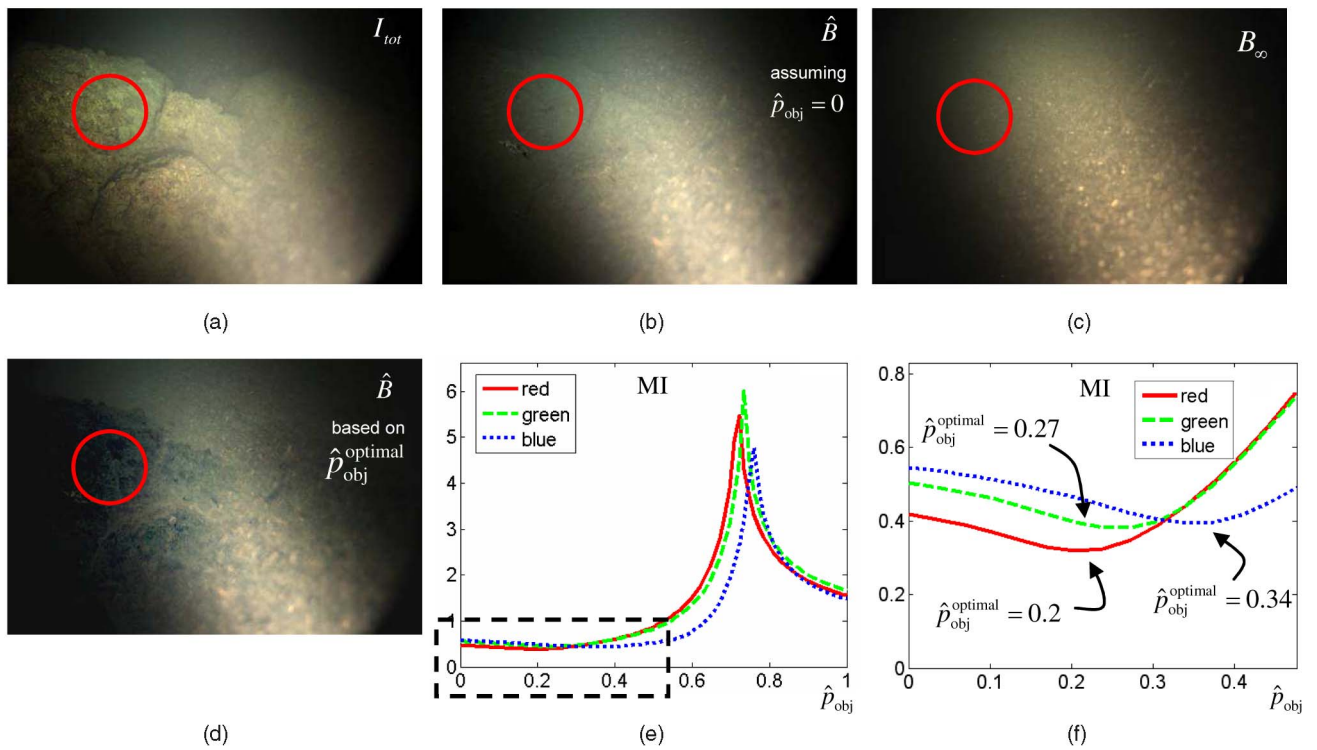


Fig. 14. (a) A raw image I of an underwater scene. (b) The estimated \hat{B} using the assumption that $\hat{p}_{obj} = 0$. (c) B_∞ of that setup. (d) \hat{B} using an estimation for \hat{p}_{obj} . (e) The MI of \hat{B} and \hat{S} as a function of \hat{p}_{obj} . In each color channel, the minimum of the MI sets $\hat{p}_{obj}^{optimal}$. (f) Zoom into the marked part of plot (e).

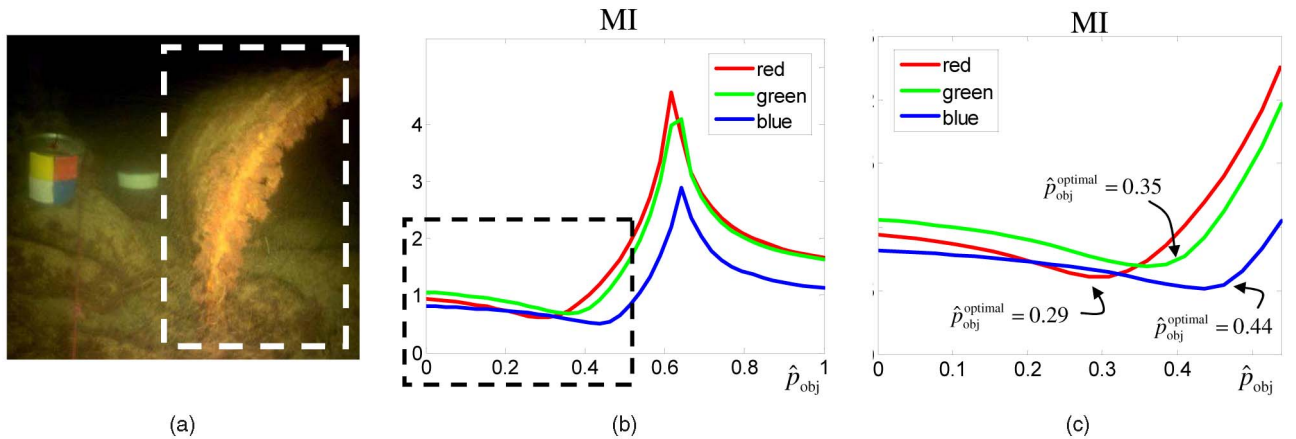


Fig. 15. Using (36) on the example in Fig. 9. The MI was calculated only on the part marked by the white rectangle in (a) to avoid the anomalous objects on the left part of (a). The full plot is shown in (b). Zoom-in of the marked rectangle in (b) is shown in (c).

6.2.1 Automatic Estimation

We discuss here an automatic approach for the estimation of p_{obj} . It is based on the observation that using a wrong value for p_{obj} increases the crosstalk between the estimated backscatter \hat{B} and the signal component \hat{S} . Let

$$\hat{p}_{obj} = p_{obj}^{true} + \varepsilon, \quad (33)$$

where ε is the error in p_{obj} . Using (33) in (12) and (13) yields an erroneous estimate of \tilde{B} :

$$\tilde{B} = B - \frac{\varepsilon}{p_{scat} - p_{obj}^{true}} \tilde{S}, \quad (34)$$

where \tilde{S} is the erroneous estimate of S . Note that (17) is a special case of (34) in which $p_{obj}^{true} = p_{obj}$ and $\varepsilon = -p_{obj}$. In any case, (34) shows that there is crosstalk between \tilde{B} and \tilde{S} that increases with ε . For example, Fig. 14b shows \hat{B} calculated using the assumption that $p_{obj} = 0$ (15). Note that the value of \hat{B} in the circled area is high. In fact, a rock from I can be seen there. Fig. 14c shows B_∞ for this setup. The value of the circled part in \hat{B} is almost as high as its value in B_∞ . This falsely indicates a far object.

To quantify the crosstalk, we may use mutual information (MI). The MI is a quantity that measures mutual statistical dependency of the two random variables \tilde{B} and \tilde{S} . A high value indicates some statistical dependency between

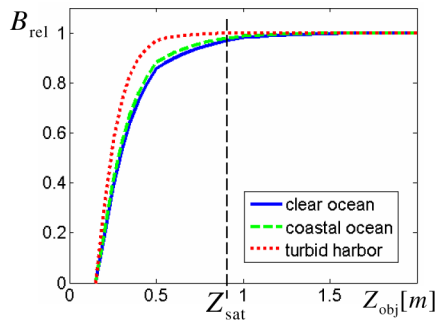


Fig. 16. The relative backscatter B_{rel} as a function of the object distance. The values for b and c are taken from [28]. The backscatter saturates within a range of 1.5 m. Moreover, the saturation distance Z_{sat} is similar in all three different water types.

the variables. Define b as a gray level in the image $\tilde{\mathbf{B}}$. Similarly, define s as a gray level in the image $\tilde{\mathbf{S}}$. Then,

$$\text{MI}(\tilde{\mathbf{B}}, \tilde{\mathbf{S}}) = \sum_{b \in \tilde{\mathbf{B}}} \sum_{s \in \tilde{\mathbf{S}}} \text{prob}(b, s) \log \left[\frac{\text{prob}(b, s)}{\text{prob}(b)\text{prob}(s)} \right], \quad (35)$$

where $\text{prob}(b, s)$ is the joint probability distribution function of pixels in $\tilde{\mathbf{B}}$ and $\tilde{\mathbf{S}}$. The marginal distribution functions of $\tilde{\mathbf{B}}$ and $\tilde{\mathbf{S}}$ are defined as $\text{prob}(b)$ and $\text{prob}(s)$, respectively. The true distribution functions are unknown and, therefore, they are estimated using histograms or, more efficiently, by Parzen windows [46]. Thus, we estimate an optimal value for \hat{p}_{obj} as

$$\hat{p}_{\text{obj}}^{\text{optimal}} = \arg \min_{\hat{p}_{\text{obj}} \in [0,1]} \{ \text{MI}[\tilde{\mathbf{B}}(\hat{p}_{\text{obj}}), \tilde{\mathbf{S}}(\hat{p}_{\text{obj}})] \}. \quad (36)$$

In the experiment shown in Fig. 14, the MI for different potential values of \hat{p}_{obj} is plotted in Figs. 14e and 14f. In each color channel, there is one value of \hat{p}_{obj} that minimizes the MI. Note that these values are *very close* to the values acquired by sampling (32). These values were used in (13) to calculate $\hat{\mathbf{B}}$ in Fig. 14d. It shows $\hat{\mathbf{B}}$ based on (13), using the value $\hat{p}_{\text{obj}}^{\text{optimal}}$ derived by (36). Now, the circled part has a low value of \hat{B} , as expected from a close object. Another example for the automatic estimation is shown in Fig. 15.

The problem becomes more complicated when p_{obj} varies across the scene. In Fig. 12, we can see (in blue ellipses) two objects whose p_{obj} is significantly different than the rest of the objects. It causes distortions in the backscatter image. In this case, we assigned for these objects the value of \hat{B}_{rel} of their surrounding in order to get an estimation of the distance map, which is shown in Fig. 9.

7 EFFECTIVENESS UNDER NOISE

Sections 4, 5, and 6 described methods to recover the object visibility and distance. An important question to ask is how distant can objects be and still be recovered? Even in a nonscattering medium, wide-field illumination is limited by the free-space falloff term $1/R_{\text{source}}^2$. This poses an inherent limit on all approaches that use wide-field illumination. Objects at long distances which are not lit effectively cannot be reconstructed. Moreover, no imaging system is free of noise. As a consequence, when the signal is in the order of

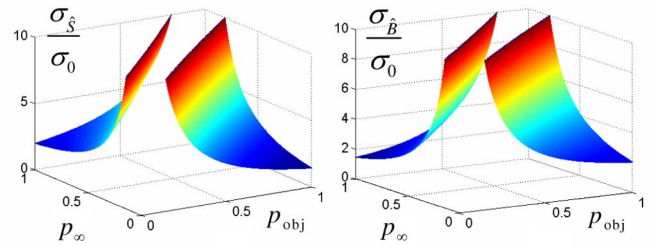


Fig. 17. The noise STDs $\sigma_{\hat{B}}$ and $\sigma_{\hat{S}}$ as a function of σ_0 , p_{obj} , and p_{scat} . The diagonal $p_{\text{obj}} = p_{\text{scat}}$ is unstable and, therefore, it is cut from the illustration.

the noise, reconstruction is limited. For example, in our system, the recorded intensity of objects farther than 6-7 m was too low to be recovered by removing the backscatter component.

As for distance recovery, a major concern is the resolution of the function $\hat{B}(Z_{\text{obj}})$. The function in (21) is approximately linear at short distances, yielding a good distance resolution. However, (21) saturates very quickly, thus losing the capacity of proper recovery. Again, when the resolution is in the magnitude of the noise, the reconstruction may become fruitless. What are the typical saturation distances? Fig. 16 depicts B_{rel} as a function of the object distance. It is a result of simulations based on three classes of values for b and c , taken from [28], which are typical of seawater at different environments. The simulated light source was placed 15 cm from the optical axis of the camera. Recall (Section 2) that the saturation distance z_{sat} is the distance in which B effectively becomes indistinguishable from B_{∞} . We can see that z_{sat} does not vary much with the water properties. In either case, beyond ≈ 1.5 m the backscatter is already saturated and is thus uninformative with respect to Z_{obj} . Therefore, accurate distance reconstruction based on backscatter is limited to the close distances. Moreover, in all of the simulated water types, $Z_{\text{sat}} \ll c^{-1}$. Sections 7.1 and 7.2 analyze the limits as a function of various medium and imaging parameters.

7.1 \hat{S} and \hat{B}

Suppose we have two statistically independent intensity measurements, I_{max} and I_{min} , with noise variances $\sigma_{I_{\text{max}}}^2$ and $\sigma_{I_{\text{min}}}^2$, respectively. Let variable v be a function of I_{max} and I_{min} . Then, in a first order approximation, the noise variance of v is given by

$$\sigma_v^2 = \left(\frac{\partial v}{\partial I_{\text{min}}} \right)^2 \sigma_{I_{\text{min}}}^2 + \left(\frac{\partial v}{\partial I_{\text{max}}} \right)^2 \sigma_{I_{\text{max}}}^2. \quad (37)$$

According to (12) and (13), the variables \hat{S} and \hat{B} linearly depend on I_{min} and I_{max} . Therefore, with respect to these variables, (37) is an exact expression. Following (12) and (13), the noise variances in \hat{S} and \hat{B} are

$$\sigma_{\hat{S}}^2 = \left(\frac{1 + p_{\text{scat}}}{p_{\text{obj}} - p_{\text{scat}}} \right)^2 \sigma_{I_{\text{min}}}^2 + \left(\frac{1 - p_{\text{scat}}}{p_{\text{obj}} - p_{\text{scat}}} \right)^2 \sigma_{I_{\text{max}}}^2, \quad (38)$$

$$\sigma_B^2 = \left(\frac{1 + p_{\text{obj}}}{p_{\text{obj}} - p_{\text{scat}}} \right)^2 \sigma_{I_{\text{min}}}^2 + \left(\frac{1 - p_{\text{obj}}}{p_{\text{obj}} - p_{\text{scat}}} \right)^2 \sigma_{I_{\text{max}}}^2. \quad (39)$$

It is obvious that if $p_{\text{obj}} \approx p_{\text{scat}}$, then $\{\sigma_{\hat{S}}, \sigma_B\} \rightarrow \infty$; hence, the reconstruction is unstable. Thus, the method works best if the medium and object differ significantly in their DOPs. Specifically, in a medium where p_{scat} is relatively high (usually in good visibility), the method works best with depolarizing objects. On the other hand, in a strongly depolarizing medium (low p_{scat}), objects are reconstructed better if they are polarizing. Note that, in (38) and (39), the noise component due to I_{min} is amplified more than that of I_{max} . For example, consider $\sigma_{\hat{S}}^2$. If $p_{\text{scat}} = 0.5$, then $\sigma_{I_{\text{min}}}^2$ is amplified nine times more than $\sigma_{I_{\text{max}}}^2$.

Let us look for a moment on a case where signal-independent noise dominates. Then, $\sigma_{I_{\text{max}}} = \sigma_{I_{\text{min}}} = \sigma_0$ and

$$\sigma_{\hat{S}}^2 = 2\sigma_0^2 \left[\frac{1 + p_{\text{scat}}^2}{(p_{\text{obj}} - p_{\text{scat}})^2} \right], \quad \sigma_B^2 = 2\sigma_0^2 \left[\frac{1 + p_{\text{obj}}^2}{(p_{\text{obj}} - p_{\text{scat}})^2} \right]. \quad (40)$$

Fig. 17 depicts $\sigma_{\hat{S}}/\sigma_0$ and σ_B/σ_0 as derived in (40). The cases $[p_{\text{scat}}, p_{\text{obj}}] = [0, 1]$ and $[p_{\text{scat}}, p_{\text{obj}}] = [1, 0]$ are two local minima. In other words, it is preferable that polarization of either the backscatter or the backreflection would be high and exclusive. In any case, $\{\sigma_B, \sigma_{\hat{S}}\} > 1$, i.e., the noise is amplified.

In reality, $\sigma_{I_{\text{max}}} \neq \sigma_{I_{\text{min}}}$ due to photon noise. Define g_{electr} as the number of photogenerated electrons required to change a unit gray level. Following [34], [42], the noise variance of a pixel gray level in an image I can be modeled as

$$\sigma_I^2 = \rho^2/g_{\text{electr}}^2 + Dt/g_{\text{electr}}^2 + \frac{I(\mathbf{x}_{\text{obj}})}{g_{\text{electr}}}, \quad (41)$$

where ρ is the STD of the electronic readout noise, induced by electronic circuitry in the camera system. It is measured as a number e^- of electrons. Here, t is the exposure time, while D is the detector dark current in units of e^-/s . In (41), the first two terms are *signal independent*. The third term is photon noise, which is *signal dependent*. As in [42], the signal-independent components are encompassed into a single term:

$$\kappa_{\text{gray}}^2 = \rho^2/g_{\text{electr}}^2 + Dt/g_{\text{electr}}^2, \quad (42)$$

assuming the same exposure time for all frames. Plugging (41) and (42) into (38) and (39) yields

$$\sigma_{\hat{S}}^2(\mathbf{x}_{\text{obj}}) = \left(\frac{1 + p_{\text{scat}}}{p_{\text{obj}} - p_{\text{scat}}} \right)^2 \left[\kappa_{\text{gray}}^2 + \frac{I_{\text{min}}(\mathbf{x}_{\text{obj}})}{g_{\text{electr}}} \right] + \left(\frac{1 - p_{\text{scat}}}{p_{\text{obj}} - p_{\text{scat}}} \right)^2 \left[\kappa_{\text{gray}}^2 + \frac{I_{\text{max}}(\mathbf{x}_{\text{obj}})}{g_{\text{electr}}} \right], \quad (43)$$

$$\sigma_B^2(\mathbf{x}_{\text{obj}}) = \left(\frac{1 + p_{\text{obj}}}{p_{\text{obj}} - p_{\text{scat}}} \right)^2 \left[\kappa_{\text{gray}}^2 + \frac{I_{\text{min}}(\mathbf{x}_{\text{obj}})}{g_{\text{electr}}} \right] + \left(\frac{1 - p_{\text{obj}}}{p_{\text{obj}} - p_{\text{scat}}} \right)^2 \left[\kappa_{\text{gray}}^2 + \frac{I_{\text{max}}(\mathbf{x}_{\text{obj}})}{g_{\text{electr}}} \right]. \quad (44)$$

Let us look at the case where $p_{\text{obj}} = 0$. From (16), (43) then becomes

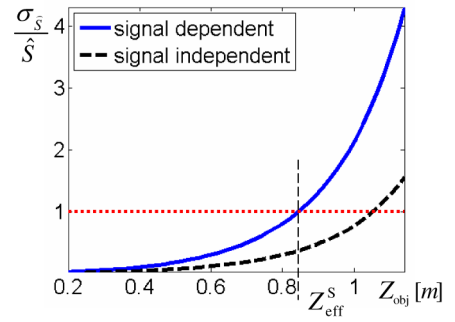


Fig. 18. STD of the reconstruction noise of \hat{S} as a function of Z_{obj} . The effective distance Z_{eff}^S is defined as the distance beyond which the noise STD in \hat{S} is greater than \hat{S} itself. In this case, it is in the order of a meter.

$$\sigma_{\hat{S}}^2(\mathbf{x}_{\text{obj}}) = \frac{1}{p_{\text{scat}}^2} \cdot \left\{ \left[2\kappa_{\text{gray}}^2 + \frac{S(\mathbf{x}_{\text{obj}})}{g_{\text{electr}}} \right] (1 + p_{\text{scat}}^2) + \frac{B(\mathbf{x}_{\text{obj}})}{g_{\text{electr}}} (1 - p_{\text{scat}}^2) \right\}. \quad (45)$$

Interestingly, $\sigma_{\hat{S}}^2$ increases with the backscatter component \mathbf{B} . Therefore, it is beneficial to reduce \mathbf{B} during acquisition. We can further use (5), (21), and (45) to approximate⁷ the dependency of $\sigma_{\hat{S}}$ on Z_{obj} :

$$\sigma_{\hat{S}}^2(\mathbf{x}_{\text{obj}}) = \frac{1}{p_{\text{scat}}^2} \cdot \left\{ \frac{B_{\infty} \{1 - \exp[-k(Z_{\text{obj}} - Z_0)]\}}{g_{\text{electr}}} (1 - p_{\text{scat}}^2) + \left[2\kappa_{\text{gray}}^2 + \frac{L_{\text{obj}}(\mathbf{x}_{\text{obj}}) \exp[-2cZ_{\text{obj}}]}{g_{\text{electr}} Z_{\text{obj}}^2} \right] (1 + p_{\text{scat}}^2) \right\}. \quad (46)$$

We define the *effective reconstruction distance* Z_{eff}^S as the distance for which

$$\frac{\sigma_{\hat{S}}(Z_{\text{eff}}^S)}{\hat{S}(Z_{\text{eff}}^S)} \approx 1. \quad (47)$$

This is the distance beyond which the noise STD in \hat{S} is greater than \hat{S} itself. Note that, when the signal-dependent component is negligible compared to κ_{gray}^2 , then (46) degenerates to (40) by substituting $\sigma_0 = \kappa_{\text{gray}}$ and $p_{\text{obj}} = 0$.

To gain insight into the dependency of $\sigma_{\hat{S}}$ on Z_{obj} , we numerically assess two cases. The first takes into consideration only the signal-independent noise κ_{gray} . The second case accounts for all noise effects [the model of (41)]. Let $B_{\infty} = 250$, i.e., close to saturation in an 8-bit camera. Assume a moderate⁸ value for the DOP, $p_{\text{scat}} = 0.6$ and attenuation coefficient $c = 0.2 \text{ m}^{-1}$. Furthermore, we set $Z_0 = 0.2 \text{ m}$, which is a typical value derived in simulations of setups where the light source is in proximity to the camera. For acquisition noise, we use typical values from [42]: $\kappa_{\text{gray}} = 0.4$, $g_{\text{electr}} = 50$. Based on these values, we assess (46) with these values. The results are shown in Fig. 18. Clearly, when taking into consideration photon noise, Z_{eff}^S shortens. We note that

7. For the falloff calculation in (46), we assumed the simple case of collinearity of the camera and the light source axis. Equation (46) also assumes a uniform light source.

8. This DOP value was chosen following our experiments, as described in Section 4.2.

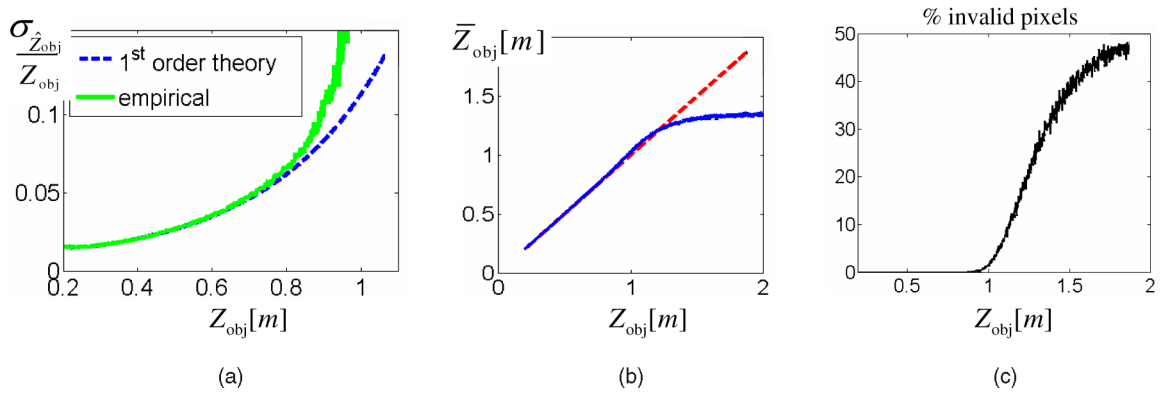


Fig. 19. (a) The value of $\sigma_{\hat{Z}_{\text{obj}}}/Z_{\text{obj}}$ in the range $Z_{\text{obj}} = [0, 1]$; theoretical first order (dashed) and empirical (solid). (b) The expected distance reconstruction $\bar{Z}_{\text{obj}}(z)$ (solid) based on valid pixels, in comparison to the utopian output Z_{obj} (dashed). (c) Percentage of the invalid pixels ($1 - |\Omega_z|/N_z$) as a function of Z_{obj} . In these pixels, $\hat{B}_{\text{rel}} \geq 1$.

we repeated this analysis for different setups of camera/light source and types of water. Changing the setup hardly changes Z_{eff}^S . However, increasing the visibility (decreasing c) increases Z_{eff}^S a little. In any case, Z_{eff}^S is in the order of a few meters. Apparently, this result does not fit our experiments, where we reconstructed objects up to 5-6 m. However, our simulation suggests that whereas the objects' visibility is enhanced by the reconstructions, the quantitative radiance values may be inaccurate.

7.2 Noise in \hat{Z}_{obj}

In Section 5.1, the distance map \hat{Z}_{obj} is estimated based on \hat{B} . Here, we analyze the effectiveness of the estimation. The noise in the estimated \hat{B} is uncorrelated with the noise in B_∞ , as both are based on different measurements. Therefore, in analogy to (37), the noise variance in the estimated distance is

$$\sigma_{\hat{Z}_{\text{obj}}}^2 = \left(\frac{\partial \hat{Z}_{\text{obj}}}{\partial \hat{B}} \right)^2 \sigma_{\hat{B}}^2 + \left(\frac{\partial \hat{Z}_{\text{obj}}}{\partial B_\infty} \right)^2 \sigma_{B_\infty}^2, \quad (48)$$

in first-order approximation. The value of B_∞ does not change between frames. Thus, it can be calibrated accurately once, setting $\sigma_{B_\infty}^2 \approx 0$. From (22),

$$\frac{\partial \hat{Z}_{\text{obj}}}{\partial \hat{B}} = \left[\frac{1}{k(1 - B_{\text{rel}})} \right] \frac{1}{B_\infty}. \quad (49)$$

Hence,

$$\sigma_{\hat{Z}_{\text{obj}}}^2 = \left[\frac{1}{k(1 - B_{\text{rel}})B_\infty} \right]^2 \sigma_{\hat{B}}^2 = \frac{\exp[2k(Z_{\text{obj}} - Z_0)]}{k^2 B_0^2} \sigma_{\hat{B}}^2, \quad (50)$$

where $\sigma_{\hat{B}}^2$ is given by (44). As expected, $\sigma_{\hat{Z}_{\text{obj}}} \rightarrow \infty$, i.e., the noise is greatly amplified as $B_{\text{rel}} \rightarrow 1$, i.e., when $Z_{\text{obj}} \gg Z_0$, destabilizing the reconstruction. However, this exponential amplification breaks the first-order approximation in (37) and (48). Thus, (50) is valid only at small values of Z_{obj} . Beyond that range, the effect of noise cannot be based on (48), and it is thus assessed numerically. When Z_{obj} increases, some noisy pixels yield $\hat{B} \geq B_\infty$, contradicting the physical model. Then, $\hat{B}_{\text{rel}} \geq 1$ and the argument of the

logarithm in (22) is either 0 or negative. This yields values of \hat{Z}_{obj} that are not physical (complex values). Having even a single pixel of such nature invalidates the variance calculation and, therefore, $\sigma_{\hat{Z}_{\text{obj}}}$ is undefined in that range.

To assess the effect of noise with respect to ground truth data, we performed numerical simulations. We simulated the acquisition process described in Section 4 using the model from Section 2. Noise was added to the simulated images to obtain I_{min} and I_{max} . Then, the distance \hat{Z}_{obj} (which is now noisy) is reconstructed from I_{min} and I_{max} using (13) and (22). We used the same parameters as in Section 7.1, $I_{\text{max}}, I_{\text{min}} \in [0, 255]$ and $p_{\text{obj}} = 0$. Fig. 19a plots $\sigma_{\hat{Z}_{\text{obj}}}/Z_{\text{obj}}$ in the range $Z_{\text{obj}} = [0, 1]$ m. The solid line shows the empirical noise variance obtained in the numerical simulation. At small values of Z_{obj} , it is consistent with the first-order theoretical approximation (50), which is plotted as a dashed curve. When Z_{obj} increases, the actual noise grows beyond the first-order calculation.

As written above, at large distances the empirical $\sigma_{\hat{Z}_{\text{obj}}}$ is undefined. Thus, in large distances, we assess the effect of noise using other measures. Let us define Ω_z as the set of all physically valid pixels located in the same distance z :

$$\Omega_z = \{ \mathbf{x} : \hat{B}_{\text{rel}}(\mathbf{x}) < 1, Z_{\text{obj}}(\mathbf{x}) = z \}. \quad (51)$$

The average estimated distance in the set Ω_z is

$$\bar{Z}_{\text{obj}}(z) = \frac{1}{|\Omega_z|} \sum_{\mathbf{x} \in \Omega_z} \hat{Z}_{\text{obj}}(\mathbf{x}). \quad (52)$$

The average $\bar{Z}_{\text{obj}}(z)$ is regarded as the expected distance reconstruction for pixels corresponding to distance $Z_{\text{obj}} = z$. We estimated $\bar{Z}_{\text{obj}}(z)$ in the simulation whose parameters are described above. For this case, Fig. 19b plots $\bar{Z}_{\text{obj}}(z)$ as a function of Z_{obj} . The distance estimation is in agreement with the ground truth up to a distance of ~ 1 m. At some point, \bar{Z}_{obj} effectively does not change with Z_{obj} . We term the distance where it happens $Z_{\text{eff}}^{Z_{\text{obj}}}$, beyond which the distance estimation becomes meaningless. This short range can be observed in Fig. 9. The bucket in the middle of the scene is placed in $Z_{\text{obj}} \approx 2$ m. As expected, the value of B_{rel} at the bucket is saturated, and thus, the bucket appears as having the same distance as the background. Fig. 19c plots $1 - |\Omega_z|/N_z$, where N_z is the total number of pixels (both

valid and invalid) corresponding to the true distance z . This is the percentage of the physically invalid pixels, i.e., where $\hat{B}_{\text{rel}} \geq 1$. Above $Z_{\text{obj}} \approx 1$ m, this percentage increases rapidly, which is in agreement with the loss of accuracy shown in Fig. 19b.

8 SUMMARY

We have presented a polarization-based method for visibility enhancement and distance estimation in scattering media. The method was demonstrated in real-life experiments. Our method uses two frames taken with wide-field polarized illumination. Therefore, it is fast and simple. We use wideband light sources, enabling colorful results. The visibility enhancement range depends on the range of the light source. However, underwater, the distance reconstruction is effective only in a range of 1-2 m. In the future, it would be beneficial to expand the work to deal with objects whose reflectance has spatially varying p_{obj} . While we performed experiments in the underwater domain, the formulation of most of our problems is general and may thus be applicable to other media. This work can be incorporated together with other methods for vision in scattering media [12].

The analysis in this paper used the single scattering approximation. In principle, multiple scattering may occur. At least in one of our experiments (Sea of Galilee, Fig. 7a), multiple scattering was significant, creating noticeable blur. Our method still resulted in visibility enhancement. Nevertheless, it will be beneficial to analyze the effects caused by multiple scattering on the methods we presented in this paper.

APPENDIX

At the current stage of the research, we wanted to reduce the effects that can potentially disturb the experimental demonstration. Hence, we had several considerations for choosing the light sources, beyond being watertight in the underwater depth:

- **Stability.** We had to avoid uncontrolled illumination fluctuations in this research phase. Hence, we avoided current arc-based flash bulbs, which have $\mathcal{O}(5\%)$ fluctuations [13]. DC incandescent sources are least prone to short-term fluctuations, once their temperature saturates.
- **Narrow lamphead exit aperture** enables fitting of high quality filters. Hence, we avoided current large LED clusters or fluorescent bulbs.
- **Holographic diffusers** are used for higher transmission efficiency and smaller diffusing angles than ground glass diffusers.
- **Sealed diffuser.** High efficiency diffusers are either ground/sandblasted glass or holographic. The former become clear (nondiffusing) in water as their refractive index is nearly matched by water in their concavities. The latter are destroyed in water. Thus, we sealed the diffusers in air-spaced windows.
- **Diffuser before polarizer.** Diffusers scramble light, causing depolarization. Laboratory tests verified a higher illumination DOP when the diffuser is placed

between the polarizer and the lamphead rather than facing the object.

- **High intensity** extends the vision range in the water.
- **Enough battery power** to last for long underwater experiments with fast recharging in field use.

We used the Aquavideo SuperNova system. It projects up to 400 W by two incandescent bulbs. A lower power of 80 W lasts for about an hour. It has a 50 mm lamphead exit. The above considerations stemmed from research needs. In a system for routine use, part of these considerations may be relaxed.

ACKNOWLEDGMENTS

The authors would like to thank Dori Yelin, Haim Kermay, Ben Herzberg, and, above all, Einav Namer for their help in the experimental dives. The authors would also like to thank Nadav Shashar for fruitful discussions and great help. Yoav Schechner is a Landau Fellow, supported by the Taub Foundation, and an Alon Fellow. This work was supported by the Israeli Science Foundation (Grant 315/04) and by the Ollendorff Center in the Department of Electrical Engineering, Technion. Tali Treibitz is funded through the BMBF.

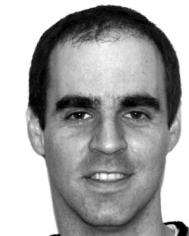
REFERENCES

- [1] P. Barham, L. Andreone, X.H. Zhang, and M. Vaché, "The Development of a Driver Vision Support System Using Far Infrared Technology: Progress to Date on the Darwin Project," *Proc. IEEE Intelligent Vehicles Symp.*, pp. 545-549, 2000.
- [2] M. Ben-Ezra, "Segmentation with Invisible Keying Signal," *Proc. IEEE Conf. Computer Vision and Pattern Recognition*, vol. 1, pp. 32-37, 2000.
- [3] T. Chen, H.P.A. Lensch, C. Fuchs, and H.P. Seidel, "Polarization and Phase-Shifting for 3D Scanning of Translucent Objects," *Proc. IEEE Conf. Computer Vision and Pattern Recognition*, 2007.
- [4] F. Cozman and E. Kroktov, "Depth from Scattering," *Proc. IEEE Conf. Computer Vision and Pattern Recognition*, pp. 801-806, 1997.
- [5] O.G. Cula, K.J. Dana, D.K. Pai, and D. Wang, "Polarization Multiplexing for Bidirectional Imaging," *Proc. IEEE Conf. Computer Vision and Pattern Recognition*, vol. 2, pp. 1116-1123, 2005.
- [6] S.G. Demos and R.R. Alfano, "Temporal Gating in Highly Scattering Media by the Degree of Optical Polarization," *Optics Letters*, vol. 21, pp. 161-163, 1996.
- [7] Y. Diamant and Y.Y. Schechner, "Overcoming Visual Reverberations," *Proc. IEEE Conf. Computer Vision and Pattern Recognition*, 2008.
- [8] H. Farid and E.H. Adelson, "Separating Reflections from Images by Use of Independent Component Analysis," *J. Optical Soc. Am. A*, vol. 16, pp. 2136-2145, 1999.
- [9] G.R. Fournier, D. Bonnier, L.J. Forand, and P.W. Pace, "Range-Gated Underwater Laser Imaging System," *Optical Eng.*, vol. 32, pp. 2185-2190, 1993.
- [10] G.C. Giakos, "Active Backscattered Optical Polarimetric Imaging of Scattered Targets," *Proc. IEEE Instrumentation and Measurement Technology Conf.*, vol. 1, pp. 430-432, 2004.
- [11] G.D. Gilbert and J.C. Pernicka, "Improvement of Underwater Visibility by Reduction of Backscatter with a Circular Polarization Technique," *Applied Optics*, vol. 6, pp. 741-746, 1967.
- [12] M. Gupta, S. Narasimhan, and Y.Y. Schechner, "On Controlling Light Transport in Poor Visibility Environments," *Proc. IEEE Conf. Computer Vision and Pattern Recognition*, 2008.
- [13] Xenon Flash Lamps, Hamamatsu, Catalog TLSX1008E04 (Hamamatsu Photonics K.K., Electron Tube Center), 1998.
- [14] S. Harsdorf, R. Reuter, and S. Töneböen, "Contrast-Enhanced Optical Imaging of Submersible Targets," *Proc. SPIE*, vol. 3821, pp. 378-383, 1999.
- [15] E.S. Harvey and M.R. Shortis, "Calibration Stability of an Underwater Stereo-Video System: Implications for Measurement Accuracy and Precision," *Marine Technology Soc. J.*, vol. 32, no. 2, pp. 3-17, 1998.

- [16] S.L. Jacques, J.C. Ramella-Roman, and K. Lee, "Imaging Skin Pathology with Polarized Light," *J. Biomedical Optics*, vol. 7, pp. 329-340, 2002.
- [17] J.S. Jaffe, "Computer Modelling and the Design of Optimal Underwater Imaging Systems," *IEEE J. Oceanic Eng.*, vol. 15, pp. 101-111, 1990.
- [18] W.S. Jagger and W.R.A. Muntz, "Aquatic Vision and the Modulation Transfer Properties of Unlighted and Diffusely Lighted Natural Waters," *Vision Research*, vol. 33, pp. 1755-1763, 1993.
- [19] G. Jarry, E. Steimer, V. Damaschini, M. Epifanie, M. Jurczak, and R. Kaiser, "Coherence and Polarization of Light Propagating through Scattering Media and Biological Tissues," *Applied Optics*, vol. 37, pp. 7357-7367, 1998.
- [20] R. Kaftory, Y.Y. Schechner, and Y.Y. Zeevi, "Variational Distance-Dependent Image Restoration," *Proc. IEEE Conf. Computer Vision and Pattern Recognition*, pp. 1-8, 2007.
- [21] D.M. Kocak and F.M. Caimi, "The Current Art of Underwater Imaging—With a Glimpse of the Past," *Marine Technology Soc. J.*, vol. 39, pp. 5-26, 2005.
- [22] A.A. Kokhanovsky, *Light Scattering Media Optics*, third ed., p. 200. Springer, 2004.
- [23] M. Levoy, B. Chen, V. Vaish, M. Horowitz, I. McDowall, and M. Bolas, "Synthetic Aperture Confocal Imaging," *ACM Trans. Graphics*, vol. 23, pp. 825-834, 2004.
- [24] G.D. Lewis, D.L. Jordan, and P.J. Roberts, "Backscattering Target Detection in a Turbid Medium by Polarization Discrimination," *Applied Optics*, vol. 38, pp. 3937-3944, 1999.
- [25] F.C. MacKintosh, J.X. Zhu, D.J. Pine, and D.A. Weitz, "Polarization Memory of Multiply Scattered Light," *Physical Rev., B*, vol. 40, no. 13, pp. 9342-9345, 1989.
- [26] B.L. McGlamery, "A Computer Model for Underwater Camera System," *Proc. SPIE*, vol. 208, pp. 221-231, 1979.
- [27] D. Miyazaki and K. Ikeuchi, "Inverse Polarization Raytracing: Estimating Surface Shape of Transparent Objects," *Proc. IEEE Conf. Computer Vision and Pattern Recognition*, vol. 2, pp. 910-917, 2005.
- [28] C.D. Mobley, *Light and Water: Radiative Transfer in Natural Waters*, chapters 3, 5. Academic Press, 1994.
- [29] S.P. Morgan and M.E. Ridgway, "Polarization Properties of Light Backscattered from a Two Layer Scattering Medium," *Optics Express*, vol. 7, pp. 395-402, 2000.
- [30] S.G. Narasimhan and S.K. Nayar, "Vision and the Atmosphere," *Int'l J. Computer Vision*, vol. 48, pp. 233-254, 2002.
- [31] S.G. Narasimhan, S.K. Nayar, B. Sun, and S.J. Koppal, "Structured Light in Scattering Media," *Proc. 10th IEEE Int'l Conf. Computer Vision*, vol. 1, pp. 420-427, 2005.
- [32] S.K. Nayar, G. Krishnan, M.D. Grossberg, and R. Raskar, "Fast Separation of Direct and Global Components of a Scene Using High Frequency Illumination," *Proc. ACM SIGGRAPH '06*, pp. 935-944, 2006.
- [33] M.J. Rakovic, G.W. Kattawar, M. Mehrubeoglu, B.D. Cameron, V. Wang, S. Rastegar, and G.L. Coté, "Light Backscattering Polarization Patterns from Turbid Media: Theory and Experiment," *Applied Optics*, vol. 38, pp. 3399-3408, 1999.
- [34] N. Ratner and Y.Y. Schechner, "Illumination Multiplexing within Fundamental Limits," *Proc. IEEE Conf. Computer Vision and Pattern Recognition*, pp. 1-8, 2007.
- [35] V. Sankaran, M.J. Everett, D.J. Maitland, and J.T. Walsh Jr., "Comparison of Polarized-Light Propagation in Biological Tissue and Phantoms," *Optics Letters*, vol. 24, pp. 1044-1046, 1999.
- [36] V. Sankaran, J.T. Walsh, and D.J. Maitland, "Comparative Study of Polarized Light Propagation in Biologic Tissues," *J. Biomedical Optics*, vol. 7, pp. 300-306, 2002.
- [37] Y.Y. Schechner and Y. Averbuch, "Regularized Image Recovery in Scattering Media," *IEEE Trans. Pattern Analysis and Machine Intelligence*, vol. 29, no. 9, pp. 1655-1660, Sept. 2007.
- [38] Y.Y. Schechner and N. Karpel, "Clear Underwater Vision," *Proc. IEEE Conf. Computer Vision and Pattern Recognition*, vol. 1, pp. 536-543, 2004.
- [39] Y.Y. Schechner and N. Karpel, "Recovery of Underwater Visibility and Structure by Polarization Analysis," *IEEE J. Oceanic Eng.*, vol. 30, pp. 570-587, 2005.
- [40] Y.Y. Schechner, S.G. Narasimhan, and S.K. Nayar, "Instant Dehazing of Images Using Polarization," *Proc. IEEE Conf. Computer Vision and Pattern Recognition*, vol. 1, pp. 325-332, 2001.
- [41] Y.Y. Schechner, S.G. Narasimhan, and S.K. Nayar, "Polarization-Based Vision through Haze," *Applied Optics*, vol. 42, pp. 511-525, 2003.
- [42] Y.Y. Schechner, S.K. Nayar, and P.N. Belhumeur, "Multiplexing for Optimal Lighting," *IEEE Trans. Pattern Analysis and Machine Intelligence*, vol. 29, no. 8, pp. 1339-1354, Aug. 2007.
- [43] Y.Y. Schechner, J. Shamir, and N. Kiryati, "Polarization and Statistical Analysis of Scenes Containing a Semi-Reflector," *J. Optical Soc. Am. A*, vol. 17, pp. 276-284, 2000.
- [44] N. Shashar, S. Sabbah, and T.W. Cronin, "Transmission of Linearly Polarized Light in Seawater: Implications for Polarization Signaling," *J. Experimental Biology*, vol. 207, pp. 3619-3628, 2004.
- [45] S. Shwartz, E. Namer, and Y.Y. Schechner, "Blind Haze Separation," *Proc. IEEE Conf. Computer Vision and Pattern Recognition*, vol. 2, pp. 1984-1991, 2006.
- [46] S. Shwartz, M. Zibulevsky, and Y.Y. Schechner, "Fast Kernel Entropy Estimation and Optimization," *Signal Processing*, vol. 85, no. 5, pp. 1045-1058, 2005.
- [47] M.P. Strand, "Imaging Model for Underwater Range-Gated Imaging Systems," *Proc. SPIE*, vol. 1537, pp. 151-160, 1991.
- [48] B. Sun, R. Ramamoorthi, S.G. Narasimhan, and S.K. Nayar, "A Practical Analytic Single Scattering Model for Real Time Rendering," *ACM Trans. Graphics*, vol. 24, pp. 1040-1049, 2005.
- [49] B.A. Swartz and J.D. Cummings, "Laser Range-Gated Underwater Imaging Including Polarization Discrimination," *Proc. SPIE*, vol. 1537, pp. 42-56, 1991.
- [50] T. Treibitz and Y.Y. Schechner, "Instant 3Descatter," *Proc. IEEE Conf. Computer Vision and Pattern Recognition*, pp. 1861-1868, 2006.
- [51] T. Treibitz, Y.Y. Schechner, and H. Singh, "Flat Refractive Geometry," *Proc. IEEE Conf. Computer Vision and Pattern Recognition*, 2008.
- [52] J.S. Tyo, M.P. Rowe, E.N. Pugh, and N. Engheta, "Target Detection in Optically Scattering Media by Polarization-Difference Imaging," *Applied Optics*, vol. 35, pp. 1855-1870, 1996.
- [53] B. Wells, "MTF Provides an Image-Quality Metric," *Laser Focus World*, vol. 41, no. 10, 2005.
- [54] L.B. Wolf, "Polarization Vision: A New Sensory Approach to Image Understanding," *Image and Vision Computing*, vol. 15, pp. 81-93, 1997.



Tali Treibitz received the BA degree in computer science from the Technion-Israel Institute of Technology in 2001, where she is currently a PhD candidate in the Department of Electrical Engineering. Her research involves physics-based computer vision. She is also an active PADI open water scuba instructor. She is a student member of the IEEE.



Yoav Y. Schechner received the BA and MSc degrees in physics and the PhD degree in electrical engineering from the Technion-Israel Institute of Technology in 1990, 1996, and 2000, respectively. During the years 2000 to 2002, he was a research scientist in the Computer Science Department at Columbia University. Since 2002, he has been a faculty member in the Department of Electrical Engineering at the Technion-Israel Institute of Technology, where he heads the Hybrid Imaging Laboratory. His research is focused on computer vision, the use of optics and physics in imaging and computer vision, and on multimodal sensing. He was the recipient of the Wolf Foundation Award for Graduate Students in 1994, the Guttwirth Special Distinction Fellowship in 1995, the Ollendorff Award in 1998, and the Morin Fellowship in 2000-2002. He is now a Landau Fellow, supported by the Taub Foundation. He has received the Klein Research Award in 2006 and the Outstanding Reviewer Awards in the IEEE Conference on Computer Vision and Pattern Recognition (CVPR '07) and the 11th IEEE International Conference on Computer Vision (ICCV '07). He is a member of the IEEE and the IEEE Computer Society.

► For more information on this or any other computing topic, please visit our Digital Library at www.computer.org/publications/dlib.